

## ARTICLE OPEN



# Electrical manipulation of a single electron spin in CMOS using a micromagnet and spin-valley coupling

Bernhard Klemt<sup>1,4</sup>, Victor Elhomsy<sup>1,4</sup>, Martin Nurizzo<sup>1</sup>, Pierre Hamonic<sup>1</sup>, Biel Martinez<sup>2</sup>, Bruna Cardoso Paz<sup>1</sup>, Cameron Spence<sup>1</sup>, Matthieu C. Dartiailh<sup>1</sup>, Baptiste Jadot<sup>3</sup>, Emmanuel Chanrion<sup>1</sup>, Vivien Thiney<sup>1</sup>, Renan Lethiecq<sup>1</sup>, Benoit Bertrand<sup>3</sup>, Heimanu Niebojewski<sup>3</sup>, Christopher Bäuerle<sup>1</sup>, Maud Vinet<sup>3</sup>, Yann-Michel Niquet<sup>2</sup>, Tristan Meunier<sup>1</sup> and Matias Urdampilleta<sup>1</sup>✉

For semiconductor spin qubits, complementary-metal-oxide-semiconductor (CMOS) technology is a promising candidate for reliable and scalable fabrication. Making the direct leap from academic fabrication to qubits fully fabricated by industrial CMOS standards is difficult without intermediate solutions. With a flexible back-end-of-line (BEOL), functionalities such as micromagnets or superconducting circuits can be added in a post-CMOS process to study the physics of these devices or achieve proofs-of-concept. Once the process is established, it can be incorporated in the foundry-compatible process flow. Here, we study a single electron spin qubit in a CMOS device with a micromagnet integrated in the flexible BEOL. We exploit the synthetic spin orbit coupling (SOC) to control the qubit via electric fields and we investigate the spin-valley physics in the presence of SOC where we show an enhancement of the Rabi frequency at the spin-valley hotspot. Finally, we probe the high frequency noise in the system using dynamical decoupling pulse sequences and demonstrate that charge noise dominates the qubit decoherence in this range.

*npj Quantum Information* (2023)9:107; <https://doi.org/10.1038/s41534-023-00776-8>

## INTRODUCTION

Foundry fabricated CMOS quantum dots offer a great opportunity to build high quality spin qubit devices with the prospect of creating a scalable quantum computer<sup>1,2</sup>. Many building blocks such as single-shot detection of electron spin states<sup>3,4</sup>, electron manipulation in small arrays<sup>5–7</sup> or single qubit operation using electron spin resonance<sup>8</sup> have been successfully implemented. However, scaling up from academic fabrication to an industrial processor requires intermediate developments. An important step is to process all the parts of the qubits that are compatible with CMOS technology on an industrial level, in order to only add the components that are not yet compatible with large scale integration by post-CMOS processing in an academic clean room. This approach allows to explore the physics of these spin qubits and characterize additional modules before their integration. Among the different modules, the development of superconducting resonators integrated in the post-CMOS process has proven to be successful in the coupling of photons with spin qubits<sup>9</sup>. Following the same principle, fabrication of magnetic materials for electric-dipole spin resonance (EDSR)<sup>10–15</sup> could also be integrated in the BEOL.

In this paper, we study the physics related to the electrical control of a single electron spin qubit using EDSR. The device is fabricated using a hybrid optical/e-beam lithography process to achieve the proof-of-concept of micromagnet integrability. We exploit the resulting synthetic SOC to drive the qubit coherently and extract its coherence properties. Moreover, we show how the presence of valleys gives rise to a second driving mechanism thanks to spin-valley mixing combined with the synthetic SOC. Finally, we use dynamical decoupling to investigate the noise source at high frequency.

## RESULTS

### Device fabrication and operation

The front-end manufacturing of the device depicted in Fig. 1a is performed in a 300 mm clean room using fully depleted silicon-on-insulator (FD-SOI) technology<sup>16</sup>, see Methods. Before the device is post-processed in an academic clean room, it is buried in 200 nm SiO<sub>2</sub> with tungsten vias to contact the gates and reservoirs. In the post-CMOS process, the alignment with respect to the tungsten vias is made by depositing a set of markers and measuring the misalignment using scanning electron microscopy (SEM). Contact is established with Ti/Al metallic lines using Electron-beam lithography (EBL) and standard lift-off techniques. The contact is ensured by an argon ion beam milling step prior to Ti/Al deposition. The Ti/Al lines are isolated from the 300 nm thick FeCo micromagnet, depicted in Fig. 1b, by 12.5 nm Al<sub>2</sub>O<sub>3</sub> grown with atomic layer deposition (ALD). Finally, the device is encapsulated with 5 nm ALD-grown Al<sub>2</sub>O<sub>3</sub> and a post-fabrication annealing is performed.

We use FeCo micromagnets with a 450 nm gap, inducing a magnetic gradient of the field component along an externally applied magnetic field ("longitudinal gradient"), and a magnetic gradient of the field components orthogonal to this external field ("transverse gradient"). The longitudinal gradient, shown in Fig. 1d, allows for individual frequency detuning<sup>17</sup>. While useful for individual qubit addressability, it also opens the door to a new dephasing channel through charge noise<sup>18,19</sup>. In the current experiment, due to misalignment during the fabrication process observed by SEM, the spin qubit quantum dot is slightly shifted away from zero longitudinal gradient, see Fig. 1d. This results in a finite dephasing gradient in the range of few MHz/nm when the electron is moved by electrical noise along the quantization axis z. Micromagnetic simulations (see Supplementary Note 1) yield a transverse gradient in the range of 0.8 mTnm<sup>-1</sup> and it is limited by

<sup>1</sup>Univ. Grenoble Alpes, CNRS, Grenoble INP, Institut Néel, Grenoble, France. <sup>2</sup>Univ. Grenoble Alpes, CEA, IRIG, Grenoble, France. <sup>3</sup>Univ. Grenoble Alpes, CEA, Leti, Grenoble, France. <sup>4</sup>These authors contributed equally: Bernhard Klemt, Victor Elhomsy. ✉email: [matias.urdampilleta@neel.cnrs.fr](mailto:matias.urdampilleta@neel.cnrs.fr)

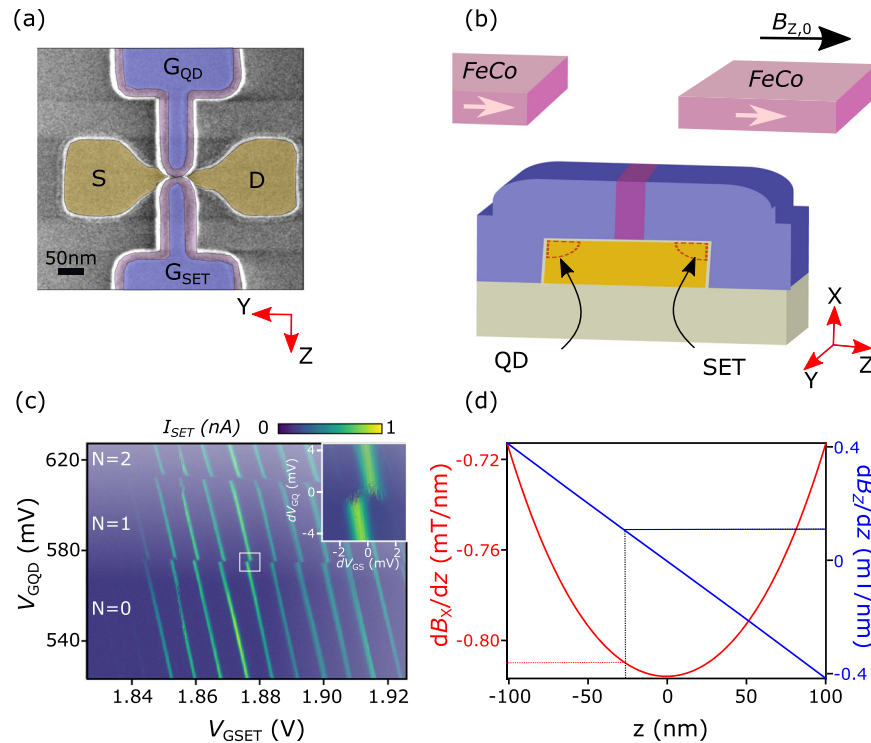


**Fig. 1 Device operation.** **a** False-coloured SEM image of a CMOS quantum dot device similar to the one used in this work. A pair of split gates (purple) is deposited on top of the channel (yellow) and SiN spacers (dark pink) are created to protect the channel from in-situ doping of the reservoirs. **b** Cut through the device along the gates, showing the position of the SET and the QD. The micromagnet added on top is magnetized by the external magnetic field  $B_{z,0}$ . **c** Stability diagram in the few electron regime for the quantum dot formed under gate  $G_{QD}$ . The current flowing through the quantum dot formed under gate  $G_{SET}$  is used for charge sensing. An abrupt shift in the conductance peak corresponds to an electron entering or leaving the QD. In the inset a zoom on the transition used for the following measurements is shown. **d** Simulation of the magnetic gradients created by the micromagnet. The transverse gradient  $dB_x/dz$  (red) and the longitudinal gradient  $dB_z/dz$  (blue) are plotted against the position across the nanowire. The gray line represents the estimated position of the QD.

the large distance between the active region of the device and the micromagnet (250 nm). The estimated stray field induced by the micromagnet is in the range of 160 mT, as it will be confirmed by Larmor spectroscopy.

Each of the two gates enables the accumulation of electrons in a so-called corner dot. The qubit dot (QD) contains a single electron whose spin is used as a qubit, and the second dot is operated as a single-electron transistor (SET) in the many electron regime<sup>3,20</sup>. To load a single electron in the QD, we start by characterizing the stability diagram of the QD-SET system as a function of the gate voltages  $G_{QD}$  and  $G_{SET}$ , see Fig. 1c. We can identify the different charge occupation regimes of the QD and perform real time measurements of tunneling events by sitting on a detector Coulomb peak at the  $N=0$  to  $N=1$  charge transition sampling data at 20 kHz (see inset of Fig. 1c).

### Spin relaxation characterization

Spin detection is performed by energy selective tunneling readout at finite magnetic field<sup>21,22</sup>. We start by emptying the qubit dot in the  $N=0$  charge region, followed by a deep plunge in the  $N=1$  charge state for a waiting time  $\tau_w$ . We then move to the measurement position: the  $N=0$  to  $N=1$  transition. We obtain a characteristic click observed in Fig. 2a. A current bump is observed when the loaded electron was in the spin-up state and the current remains at the base level when a spin-down electron was loaded. To further characterize the readout configuration, we measure the probability to find the system in the spin-up state deep in the  $N=1$  charge state, as a function of  $\tau_w$ . We obtain a characteristic relaxation curve, depicted in Fig. 2b from which we extract a relaxation time  $T_1$  of 5.2 ms. The measurement gives a limited

visibility of 75%, and is further reduced in the following of the paper, as the magnetic field is decreased leading to a smaller  $E_Z/k_B T$  ratio, with  $T$  the electron temperature (estimated to be 400 mK),  $E_Z = g\mu_B B_z$  the Zeeman energy,  $k_B$  the Boltzmann constant,  $g=2$  the  $g$ -factor of electrons in silicon, and  $\mu_B$  the Bohr magneton<sup>23</sup>.

Probing relaxation allows to extract more information about the QD spectrum and its coupling to environment<sup>24–27</sup>. In particular, the relaxation curve in Fig. 2c shows the presence of a hotspot where fast relaxation occurs (see Supplementary Note 3 for details about the fitting). This enhancement of relaxation rate is due to the presence of valley states which can mix with the spin degree of freedom. From this point we extract the valley splitting  $E_{VS} = 60 \mu\text{eV}$ . It is worth noting that this value takes into account the micromagnet stray field (see Supplementary Note 2).

### Electric-dipole spin resonance

We probe the spectrum of the spin states by performing pulsed measurements using EDSR. The EDSR drive is applied to  $G_{QD}$  with an estimated 1 mV amplitude. At fixed magnetic field, we extract the Zeeman energy from a fit of the Larmor resonance (Fig. 3a). The Larmor frequency is then studied with respect to the external magnetic field, see Supplementary Note 2. From such measurements, taking into account that  $g=2$ , the micromagnet stray field is evaluated to be in the range of 160 mT. However, the magnetization of the micromagnet is changing with the externally applied magnetic field leading to different Larmor frequencies depending on how the external magnetic field has been swept previously. Tracking the Larmor frequency as a function of the external magnetic field allows us to reconstruct its micromagnet

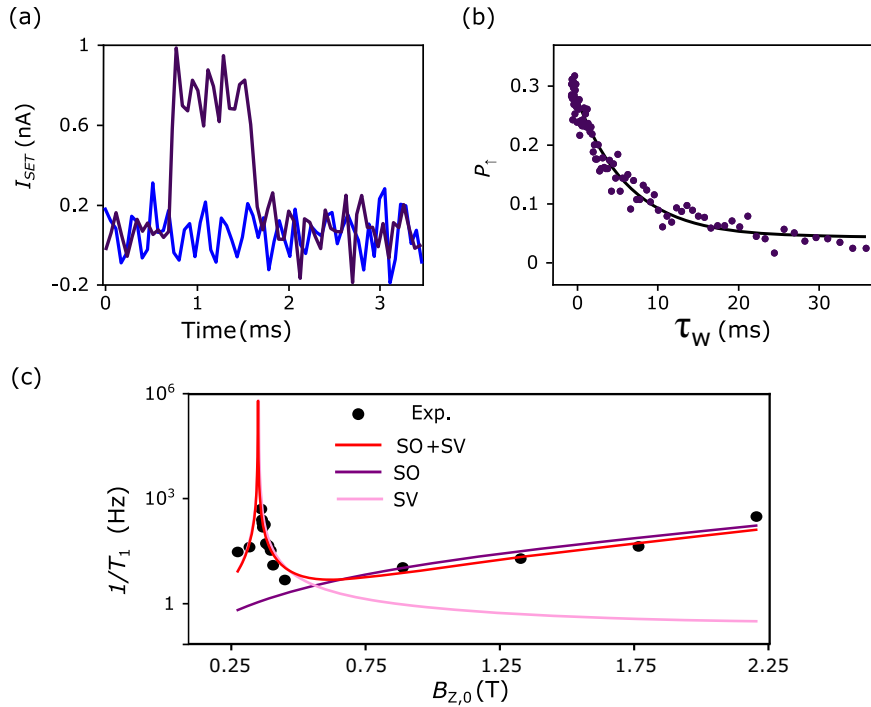


**Fig. 2 Spin relaxation characterization.** **a** Single shot traces representing typical scenarios of a spin-down electron (blue) and a spin-up electron (purple) being detected. **b** Measurement of the spin relaxation time  $T_1$ . Spin-up probability as a function of loading time is fitted to an exponential decay, yielding a spin relaxation time of  $T_1 = 5.2$  ms. The initialization is performed by loading a random spin in the quantum dot. **c** Spin relaxation rate  $1/T_1$  plotted for different externally applied magnetic fields. At an applied field of 0.36 T, an abrupt relaxation increase is visible (hotspot). It gives an estimation of the valley splitting energy  $E_{VS} = 60 \mu\text{eV}$  taking into account a micromagnet stray field of 0.167 T (see Supplementary Note 2). The data is fitted to determine the contribution of spin-orbit coupling (purple) and spin-valley coupling (pink). The combination of spin-orbit and spin-valley coupling (red) fits the data best.

minor hysteresis loop presented in Supplementary Note 2 in agreement with a partially saturated magnet.

We now use this spectroscopy to track the evolution of the qubit energy over time. For this purpose we measure the Larmor frequency over three days, and using Fourier transform we construct the noise power spectral density (PSD) curve in Fig. 3b. It shows fluctuations as strong as 10 MHz at low frequency, which is in good agreement with hyperfine interaction in natural silicon devices<sup>28</sup>. To fit the experimental data, we use a hyperfine model of nuclear spins with only three clusters in the frequency window. We obtain saturation of the PSD at very low frequency as expected for a finite number of fluctuators, but we do not reach the expected  $1/f^2$  regime at higher frequency due to the small measurement bandwidth in our case. In the following, we recalibrate the Larmor frequency every two minutes to minimize the influence of this quasi-static noise.

We now move to the coherent manipulation of the qubit. We perform Rabi oscillations by sweeping the duration of a 1 mV AC drive at the Larmor frequency  $f_0$ . We obtain the data presented in Fig. 3b, c. We observe a non-exponential decay of the Rabi oscillations which is attributed to the non-Markovian nature and slow fluctuation of the nuclear spin bath over the spin rotation time scale<sup>29</sup>. The Rabi frequency over voltage drive ratio corresponds to approximately 1 MHz per mV. It is worth noting that the drive amplitude is limited to 1 mV in the present sample due to a heating effect, reducing drastically the visibility.

Using the above calibrated rotations we perform a Hahn echo sequence. We extract the intrinsic dephasing time  $T_2^*$  from the width of the echo<sup>28</sup>, as depicted in Fig. 3d. It falls in the 500 ns range when measured over few minutes. The difference with reported values in natural silicon<sup>12,30</sup> is explained by a smaller size

of quantum dot leading to a shorter hyperfine-induced dephasing. Supplementary Fig. 2a in Supplementary Note 4 presents a calculation of the wavefunction size in the present device<sup>31</sup>. We approximate the dot volume to an ellipsoid of main axis (2 nm, 6 nm, 9 nm) giving a volume around  $400 \text{ nm}^3$  which is one order of magnitude smaller than standard SiGe quantum dots<sup>19</sup>.

### Valley enhanced EDSR

To investigate the interplay between valley mixing and synthetic SOC, we perform EDSR as a function of the magnetic field<sup>32–34</sup>. Figure 4a presents Rabi oscillations performed at different magnetic fields. It shows an increase of the Rabi frequency as the field gets closer to the valley degeneracy (hotspot). This is supported by Fig. 4b which plots both the Rabi frequency and the relaxation rate as a function of the magnetic field. It is worth noting that measurement further on the hotspot is prevented by fast relaxation during readout. This increase of EDSR Rabi frequency at the hotspot is related to the presence of a second drive mechanism which involves the presence of valley mixing in the silicon QD combined with synthetic SOC<sup>35</sup>. More precisely, the microwave electric field allows a transition from two different valleys but same spin ( $|v_-, \downarrow\rangle$  and  $|v_+, \downarrow\rangle$ ) and the synthetic SOC couples the two opposite spins in different valleys ( $|v_-, \uparrow\rangle$  and  $|v_+, \downarrow\rangle$ ) which eventually leads to an opposite spin and same valley transition ( $|v_-, \uparrow\rangle$  to  $|v_-, \downarrow\rangle$ )<sup>36</sup>.

The Rabi frequency monotonously increases with the valley mixing which indicates that the two mechanisms are adding up resulting in a larger transverse field in the rotating frame. A more quantitative estimation of the amplitude and phase of the two components of the driving fields in the rotating frame is impractical here. It would require to change both the direction of the synthetic SOC field and the external magnetic field  $B_{z,0}$  to

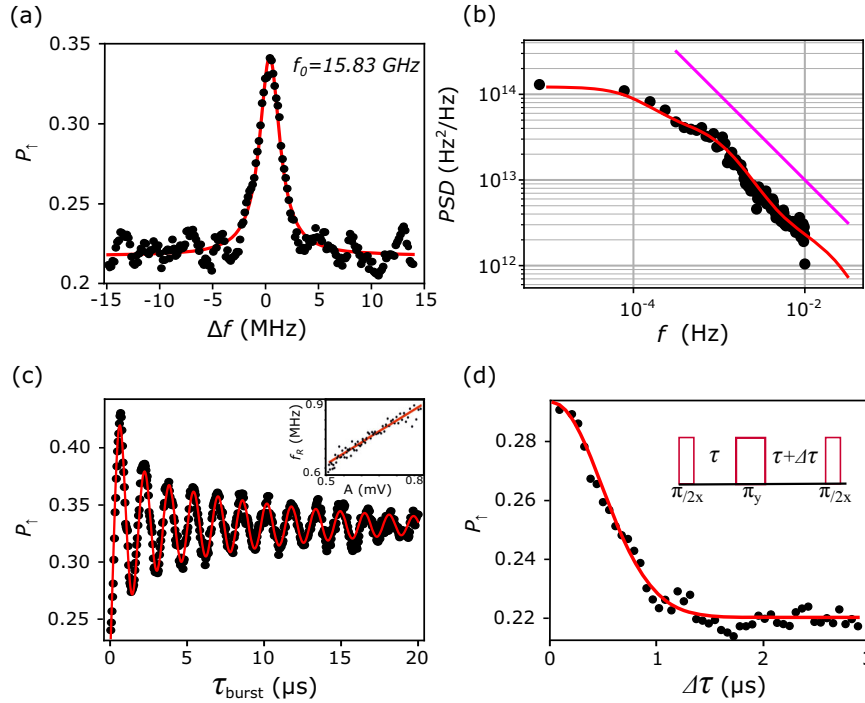


**Fig. 3 Spin coherent manipulation.** **a** EDSR spectrum of the single electron spin. Spin-up state probability is measured as a function of the excitation frequency. The peak is centered around the Larmor frequency  $f_0$ . The initialization is performed by waiting 1 ms at the measurement position where, in principle, only the ground state is accessible. **b** Power spectral density of qubit frequency. The Larmor frequency is measured over three days followed by a Fourier transform (black dots). The fit (red) corresponds to a model including three nuclear spins at different fluctuating frequencies. The  $1/f$  trend is depicted with the pink line. **c** Rabi oscillations for 1 mV excitation amplitude. The data points (black) are fitted using the  $\cos(\omega t + \pi/4)/\sqrt{t}$  function to account for the slowly fluctuating nuclear field. Inset: Rabi frequency as a function of estimated driving amplitude on the gate. **d** Echo envelope measured using a Hahn echo with evolution time of 3  $\mu\text{s}$ , leading to an estimated  $T_2^*$  of 500 ns.

map and disentangle the evolution of the two mechanisms in space. While the presence of valleys offers an enhancement of EDSR driving speed, it also increases the susceptibility of the qubit to charge noise. We observe a similar trend between the Rabi frequency and the decoherence rate of Rabi oscillations, see Supplementary Note 5. Though, we do not observe a clear enhancement of the quality factor as was proposed in ref. <sup>35</sup>. We therefore need to understand further the noise spectrum of the qubit and in particular the influence of charge noise.

### Probing high frequency charge noise using dynamical decoupling

To probe noise at higher frequency, we implement dynamical decoupling sequences starting with a Hahn echo (see Supplementary Note 6). We obtain the echo amplitude as a function of evolution time fitted with a Gaussian decay plotted in Fig. 5a (black dots) which leads to  $T_2^E = 36 \mu\text{s}$ . This is two orders of magnitude longer than  $T_2^*$  showing the efficiency of the refocusing pulse to filter out the quasi-static noise. To get rid of a larger noise spectrum, we implement Carr-Purcell-Meiboom-Gill (CPMG) pulse sequences, which consist in applying multiple  $\pi$  pulses in a given evolution time<sup>37–39</sup>. Such a pulse sequence is characterized by the number of  $\pi$  pulses  $n_\pi$ , the total free evolution time  $\tau$ , and the duration of a  $\pi$  pulse  $t_\pi$ . The total time of one CPMG experiment is then given by  $t = \tau + n_\pi t_\pi$ . The amplitudes obtained after a final refocusing  $\pi/2$  pulse are summarized in Fig. 5a. For  $n_\pi \pi$  pulses, the echo amplitude  $A(t)$  is fitted using the following equation<sup>40</sup>:

$$A^{n_\pi}(t) = \exp\left[-(t/T_2^{n_\pi})^{1+\alpha}\right] \quad (1)$$

where  $T_2^{n_\pi}$  is the characteristic CPMG time for information loss, for a given  $n_\pi$ . The parameter  $\alpha$  is the noise color.

Another way to represent this dependence is to plot the CPMG-enhanced  $T_2^{n_\pi}$  with respect to  $n_\pi$ , see Fig. 5b. The pulse number dependence follows a power law  $n_\pi^{\alpha/(\alpha+1)}$  which in our case is consistent with a noise color of around  $\alpha = 0.8$  over the frequency range of CPMG pulse repetitions ( $10^4 - 10^6 \text{ Hz}$ ). This is slightly different from typical  $\alpha = 1$  in semiconductor structures<sup>11,41</sup>, indicating that a finite ensemble of two-level systems in the surroundings of the qubit dominates the noise at higher frequencies. It is worth noting that the number  $n_\pi$  of  $\pi$  pulses is limited due to the poor gate fidelity induced by the large decoherence rate (see Supplementary Note 7).

A complementary analysis of CPMG data consists in considering these pulse sequences as tools for noise spectroscopy<sup>11,41</sup>. We are interested in the phase information of the electron spin, at times  $t$ , which we can write as:  $\langle \exp[i\phi(t)] \rangle \equiv \exp[-\chi(t)]$ , where the phase decay envelope  $\chi$  can be expressed as:

$$\chi(t) = 4\pi^2 \int_0^{+\infty} df S'_{f_0}(f) \times W(f, \tau, t_\pi, n_\pi) \quad (2)$$

Supplementary Note 8 gives details on this expression and on this section, following closely Connors et al.<sup>41</sup>. In this expression,  $S'_{f_0}(f)$  is the double-sided power spectral density (PSD) of the noise on the Larmor frequency, and  $W(f, \tau, t_\pi, n_\pi)$  is the spectral weighting function corresponding to a specific pulse sequence. The normalized amplitude  $A^{n_\pi}$  plotted in Fig. 5a embodies the loss of phase information in the corresponding CPMG experiment, giving:

$$\chi(t = \tau + n_\pi t_\pi) = -\ln[A^{n_\pi}(\tau, t_\pi, n_\pi)] \quad (3)$$

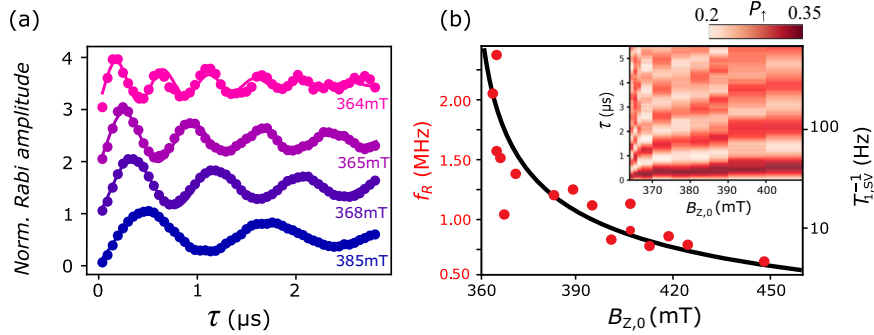


**Fig. 4 Valley-enhanced EDSR.** **a** Rabi oscillations at different magnetic fields (364, 365, 368 and 385 mT) for a constant drive amplitude ( $V_{AC} = 1$  mV). **b** Experimental Rabi frequency and relaxation rate from spin-valley model as a function of the externally applied magnetic field. The Rabi frequency follows the same trend as the spin-valley contribution of the relaxation rate by increasing in the vicinity of the spin-valley degeneracy. Inset: colormap of Rabi oscillations as a function of field.

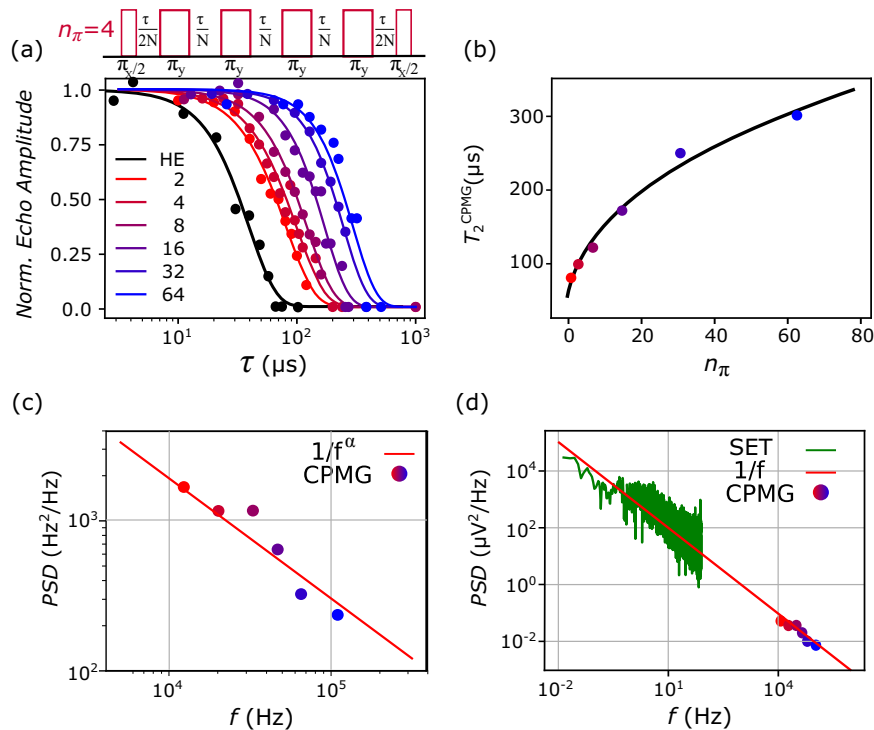


**Fig. 5 Dynamical decoupling and high frequency noise.** **a** Normalized echo amplitude as a function of total free evolution time using CPMG sequences at  $B_{z,0} = 405$  mT. These sequences are composed of a series of  $n_\pi \pi_y$  pulses, as depicted on the top of the figure for  $n_\pi = 4$  and finished with a  $\pi_x/2$  probe at different timings  $\tau + \delta\tau$ , where  $\delta\tau$  is swept to capture the whole echo. For each CPMG the echo is renormalized using the reference echo amplitude for  $\tau = 1$   $\mu$ s. The different decay curves are fitted using the following expression  $A(t) = \exp[-(t/T_2)^\beta]$  with  $\beta = 1 + \alpha$ . **b** Evolution of CPMG-enhanced  $T_2$  with number of refocusing pulses.  $T_2$  values are extracted from the decay curves in (a) and fitted using  $T_2^{n_\pi} \propto n_\pi^{\frac{\alpha}{1-\alpha}}$ . **c** Noise power spectral density of the qubit energy fluctuation for the evolution time corresponding to the CPMG  $T_2^{n_\pi}$  times. Treating the CPMG sequence as a band pass filter allows to extract the noise PSD around the pulse repetition frequency. The  $1/f$  trend, characteristic of charge noise, is plotted along the data points. **d** Noise power spectral density in terms of effective gate voltage. The low frequency data points are extracted from time domain current measurements on the flank of a SET Coulomb peak followed by Fourier transform. The high frequency points correspond to data points from (a), turned into voltage fluctuations knowing the longitudinal magnetic gradient and the charge displacement due to gate voltage.

If we assume a single-sided PSD of the form  $S_{f_0}(f) = 2S'_{f_0}(f) = C/f^\alpha$ , with  $\alpha = 0.8$  found in the last section, we can compute  $C$  for all of our CPMG experiments using equation (2). We get  $C^{n_\pi}$  values by averaging the results for  $C$  at a given  $n_\pi$ , taking into account the normalized CPMG amplitudes between 0.15 and 0.85, where the amplitude is less likely to come from instrumental errors. In order to visualize these results, we note that the spectral weighting function  $W$  peaks at  $f = n_\pi D/2\tau$ , where  $D = \tau/(\tau + n_\pi t_\pi)$  is the duty cycle of the pulse sequence. As a set of

CPMG experiments at fixed  $n_\pi$  is characterized by the time  $T_2^{n_\pi}$ , we chose to plot  $S_{f_0}(f^{n_\pi} = n_\pi D/2T_2^{n_\pi}) = C^{n_\pi}/(f^{n_\pi})^\alpha$  in Fig. 5c.

To confirm the origin of charge noise as the main source of decoherence at high frequency, we now turn the PSD  $S_{f_0}$  into a PSD  $S_V$  in terms of fluctuations of gate voltage: we mimic the effect of this charge noise by an effective noise on the gate voltage. This voltage noise translates into qubit frequency fluctuations by moving the electron along the  $z$  axis combined with a longitudinal gradient  $\frac{dB_z}{dz}$ . It summarizes with the following

expression:

$$S_{f_0} = \frac{g\mu_B}{h} \times \frac{dB_z}{dz} \times \delta_e \times S_V \quad (4)$$

where  $h$  is the Planck constant and  $\delta_e$  is the electron displacement along  $z$  due to gate voltage on  $G_{\text{OD}}$ . This displacement per voltage can be extracted from the Rabi oscillations assuming:

$$\delta_e = \frac{f_R}{V_{\text{AC}} \times \frac{g\mu_B}{h} \times \frac{dB_z}{dz}} \quad (5)$$

with  $V_{\text{AC}}$  the excitation voltage to drive Rabi oscillations at frequency  $f_R$ ,  $\frac{dB_z}{dz}$  the transverse gradient. Using equation (5) and a Rabi frequency of  $f_R = 1$  MHz for  $V_{\text{AC}} = 1$  mV, we obtain an electron displacement of 45 pm/mV. Using equation (4) we plot in Fig. 5c the PSD in terms of fluctuations in gate voltage. To compare with a standard charge noise measurement, we also add on the same plot the PSD extracted from SET fluctuations obtained by simply transforming SET current measurements recorded while sitting on the flank of a Coulomb peak. We obtain a good agreement between the high and low frequency data points falling on the  $1/f$  trend. This pink noise behavior over 6 decades confirms the origin of the decoherence mechanism at high frequency to be charge noise.

To compare with other spin qubit platforms, we can convert the PSD from Fig. 5d at 1 Hz ( $1000 \mu\text{V}^2\text{Hz}^{-1}$ ) to a PSD in terms of chemical potential using the lever arm ( $0.25\text{eV}\text{V}^{-1}$ ). We obtain  $8 \mu\text{eV}\text{Hz}^{-1/2}$ . This value is one to two orders of magnitude higher compared to commonly reported values in literature<sup>5,41,42</sup>, but similar to foundry fabricated spin qubits<sup>8</sup>. In our case, this large charge noise amplitude points toward a degradation of device quality during the post-CMOS process which uses lower standard processes. However, the high frequency fluctuations of the qubit are similar to what is reported in other platforms with less nominal charge noise while the longitudinal gradient is comparable. Therefore, we attribute the lower influence of charge noise to a small charge displacement susceptibility ( $\delta_e = 45 \text{ pmmV}^{-1}$ ) due to confinement in the corner of the nanowire.

## DISCUSSION

In conclusion, we have seen that a post-CMOS process can be used to implement additional functionalities to foundry-fabricated devices. With this process, we patterned a micromagnet on top of a CMOS device, which enabled coherent manipulation of an electron spin through electric-dipole spin resonance. We identify two driving mechanisms: the one based on bare synthetic spin-orbit coupling and the one induced by combining the spin-valley mixing near the valley hotspot with the synthetic spin-orbit coupling. We further investigate the coherent properties of the spin qubit which shows a dephasing time around 500 ns due to hyperfine coupling to surrounding nuclear spins in the small volume of the quantum dot. Refocusing this low frequency noise through dynamical decoupling pulse sequences allowed to enhance the qubit coherence time by three orders of magnitude, and provided evidence that high-frequency noise has electrical origin, with an amplitude comparable to state-of-the-art spin qubit realizations. While the charge noise amplitude is relatively high, the induced decoherence at large frequency is relatively small, due to the strong confinement in the corner of the nanowire, at the cost of lower Rabi frequency. Lowering both the hyperfine quasistatic noise thanks to isotopic purification and the charge noise by two orders of magnitude would make these CMOS-based spin qubits a promising platform for quantum information.

## METHODS

### Experimental setup

Experiments are performed in the CMOS device as shown in Fig. 1a using a dilution refrigerator with a base temperature of 120 mK. Charge sensing is performed by monitoring the current through the SET using a homemade IV converter followed by digitization using a NI BNC 2110 acquisition card. The voltage on gates is controlled using digital-to-analog converters controlled by a sbRIO-9208 FPGA board.

### Front-end device fabrication

The device, presented in Fig. 1a, is based on a 80 nm wide silicon nanowire transistor from fully depleted silicon-on-insulator (FD-SOI) technology<sup>16</sup>. On top of a 10 nm thick nanowire, 6 nm  $\text{SiO}_2$  gate oxide and 5 nm TiN/50 nm polysilicon gate metal are deposited. A single pair of split gates with a gate length and gate separation of 50 nm is patterned using optical and electron-beam lithography (EBL). SiN spacers are created to protect the device during the in situ doping of the reservoirs with phosphorus.

### DATA AVAILABILITY

All data that support the findings of this study are available from the corresponding author upon request.

Received: 28 March 2023; Accepted: 5 October 2023;

Published online: 23 October 2023

## REFERENCES

- Gonzalez-Zalba, M. et al. Scaling silicon-based quantum computing using CMOS technology. *Nat. Electron.* **4**, 872–884 (2021).
- Veldhorst, M., Eenink, H., Yang, C. & Dzurak, A. Silicon CMOS architecture for a spin-based quantum computer. *Nat. Commun.* **8**, 1766 (2017).
- Ciriano-Tejeda, V. et al. Spin readout of a CMOS quantum dot by gate reflectometry and spin-dependent tunneling. *PRX Quantum* **2**, 010353 (2021).
- Niegemann, D. et al. Parity and singlet-triplet high-fidelity readout in a silicon double quantum dot at 0.5 K. *PRX Quantum* **3**, 040335 (2022).
- Chanrion, E. et al. Charge detection in an array of CMOS quantum dots. *Phys. Rev. Appl.* **14**, 024066 (2020).
- Gilbert, W. et al. Single-electron operation of a silicon-CMOS  $2 \times 2$  quantum dot array with integrated charge sensing. *Nano Lett.* **20**, 7882–7888 (2020).
- Ansaloni, F. et al. Single-electron operations in a foundry-fabricated array of quantum dots. *Nat. Commun.* **11**, 6399 (2020).
- Zwerver, A. M. J. et al. Qubits made by advanced semiconductor manufacturing. *Nat. Electron* **5**, 184–190 (2022).
- Yu, Cécile X. et al. Strong coupling between a photon and a hole spin in silicon. *Nat. Nanotechnol.* 1–6 (2023).
- Pioro-Ladrière, M. et al. Electrically driven single-electron spin resonance in a slanting Zeeman field. *Nat. Phys.* **4**, 776–779 (2008).
- Yoneda, J. et al. A quantum-dot spin qubit with coherence limited by charge noise and fidelity higher than 99.9%. *Nat. Nanotechnol.* **13**, 102–106 (2018).
- Kawakami, E. et al. Electrical control of a long-lived spin qubit in a Si/SiGe quantum dot. *Nat. Nanotechnol.* **9**, 666–670 (2014).
- Leon, R. et al. Coherent spin control of s-, p-, d- and f-electrons in a silicon quantum dot. *Nat. Commun.* **11**, 797 (2020).
- Sigillito, A. et al. Site-selective quantum control in an isotopically enriched  $^{28}\text{Si}/\text{Si}_{0.7}\text{Ge}_{0.3}$  quadruple quantum dot. *Phys. Rev. Appl.* **11**, 061006 (2019).
- Zhang, X. et al. Controlling synthetic spin-orbit coupling in a silicon quantum dot with magnetic field. *Phys. Rev. Appl.* **15**, 044042 (2021).
- De Franceschi, S. et al. SOI technology for quantum information processing. In 2016 IEEE International Electron Devices Meeting (IEDM) (pp. 13–4). IEEE (2016).
- Phillips, S. et al. Universal control of a six-qubit quantum processor in silicon. *Nature* **609**, 919–924 (2022).
- Culcer, D., Hu, X. & Das Sarma, S. Dephasing of Si spin qubits due to charge noise. *Appl. Phys. Lett.* **95**, 73102 (2009).
- Struck, T. et al. Low-frequency spin qubit energy splitting noise in highly purified  $^{28}\text{Si}/\text{SiGe}$ . *Npj Quantum Inf.* **6**, 40 (2020).

20. Spence, C. et al. Spin-valley coupling anisotropy and noise in CMOS quantum dots. *Phys. Rev. Appl.* **17**, 034047 (2022).
21. Elzerman, J. et al. Single-shot read-out of an individual electron spin in a quantum dot. *Nature* **430**, 431–435 (2004).
22. Morello, A. et al. Single-shot readout of an electron spin in silicon. *Nature* **467**, 687–691 (2010).
23. Keith, D. et al. Benchmarking high fidelity single-shot readout of semiconductor qubits. *N. J. Phys.* **21**, 63011 (2019).
24. Zhang, X. et al. Giant anisotropy of spin relaxation and spin-valley mixing in a silicon quantum dot. *Phys. Rev. Lett.* **124**, 257701 (2020).
25. Petit, L. et al. Spin lifetime and charge noise in hot silicon quantum dot qubits. *Phys. Rev. Lett.* **121**, 076801 (2018).
26. Yang, C. et al. Spin-valley lifetimes in a silicon quantum dot with tunable valley splitting. *Nat. Commun.* **4**, 2069 (2013).
27. Huang, P. & Hu, X. Spin relaxation in a Si quantum dot due to spin-valley mixing. *Phys. Rev. B* **90**, 235315 (2014).
28. Pla, J. et al. A single-atom electron spin qubit in silicon. *Nature* **489**, 541–545 (2012).
29. Koppens, F. et al. Universal phase shift and nonexponential decay of driven single-spin oscillations. *Phys. Rev. Lett.* **99**, 106803 (2007).
30. Takeda, K. et al. A fault-tolerant addressable spin qubit in a natural silicon quantum dot. *Sci. Adv.* **2**, e1600694 (2016).
31. Martinez, B. & Niquet, Y.-M. Variability of electron and hole spin qubits due to interface roughness and charge traps. *Phys. Rev. Appl.* **24**, 024022 (2022).
32. Huang, W., Veldhorst, M., Zimmerman, N., Dzurak, A. & Culcer, D. Electrically driven spin qubit based on valley mixing. *Phys. Rev. B* **95**, 075403 (2017).
33. Corna, A. et al. Electrically driven electron spin resonance mediated by spin-valley-orbit coupling in a silicon quantum dot. *Npj Quantum Inf.* **4**, 6 (2018).
34. Hao, X. et al. Electron spin resonance and spin-valley physics in a silicon double quantum dot. *Nat. Commun.* **5**, 3860 (2014).
35. Huang, P. & Hu, X. Fast spin-valley-based quantum gates in Si with micromagnets. *Npj Quantum Inf.* **7**, 162 (2021).
36. Bourdet, L. & Niquet, Y. All-electrical manipulation of silicon spin qubits with tunable spin-valley mixing. *Phys. Rev. B* **97**, 155433 (2018).
37. Carr, H. & Purcell, E. Effects of diffusion on free precession in nuclear magnetic resonance experiments. *Phys. Rev.* **94**, 630–638 (1954).
38. Meiboom, S. & Gill, D. Modified spin echo method for measuring nuclear relaxation times. *Rev. Sci. Instrum.* **29**, 688–691 (1958).
39. Viola, L. & Lloyd, S. Dynamical suppression of decoherence in two-state quantum systems. *Phys. Rev. A* **58**, 2733–2744 (1998).
40. Kawakami, E. et al. Gate fidelity and coherence of an electron spin in an Si/SiGe quantum dot with micromagnet. *Proc. Natl Acad. Sci. USA* **113**, 11738–11743 (2016).
41. Connors, E. J. et al. Charge-noise spectroscopy of Si/SiGe quantum dots via dynamically-decoupled exchange oscillations. *Nat. Commun.* **13**, 940 (2022).
42. Kranz, L. et al. Exploiting a single-crystal environment to minimize the charge noise on qubits in silicon. *Adv. Mater.* **32**, 2003361 (2020).

## ACKNOWLEDGEMENTS

We acknowledge technical support from L. Hutin, D. Lepoittevin, I. Pheng, T. Crozes, L. Del Rey, D. Dufeu, J. Jarreau, C. Hoarau and C. Guttin. We thank S. De Franceschi and R. Maurand for fruitful discussions and I. De Moraes and N. Dempsey for help with

micromagnet fabrication. B.K., D.J.N. acknowledges the GreQuE doctoral programs (grant agreement No.754303). The device fabrication is funded through the Mosquito project (Grant agreement No.688539). This work is supported by the Agence Nationale de la Recherche through the CRYMCO and the PEPR PRESQUILE project. This project receives as well funding from the project QuCube (Grant agreement No.810504) and the project QLSI (Grant agreement No.951852).

## AUTHOR CONTRIBUTIONS

H.N., B.B., and M.V. were responsible for the front-end fabrication of the device. B.K. postprocessed the micromagnet and contacts on the CMOS device. B.K. performed measurement with help from V.E. and M.U. V.E. performed the micromagnetic simulations and CPMG analysis. B.M. performed the numerical simulations of the electron wave function. M.U., V.E., and B.K. co-wrote the manuscript with inputs from all the authors. T.M. and M.U. supervised and initiated the project.

## COMPETING INTERESTS

The authors declare no competing interests.

## ADDITIONAL INFORMATION

**Supplementary information** The online version contains supplementary material available at <https://doi.org/10.1038/s41534-023-00776-8>.

**Correspondence** and requests for materials should be addressed to Matias Urdampilleta.

**Reprints and permission information** is available at <http://www.nature.com/reprints>

**Publisher's note** Springer Nature remains neutral with regard to jurisdictional claims in published maps and institutional affiliations.



**Open Access** This article is licensed under a Creative Commons Attribution 4.0 International License, which permits use, sharing, adaptation, distribution and reproduction in any medium or format, as long as you give appropriate credit to the original author(s) and the source, provide a link to the Creative Commons license, and indicate if changes were made. The images or other third party material in this article are included in the article's Creative Commons license, unless indicated otherwise in a credit line to the material. If material is not included in the article's Creative Commons license and your intended use is not permitted by statutory regulation or exceeds the permitted use, you will need to obtain permission directly from the copyright holder. To view a copy of this license, visit <http://creativecommons.org/licenses/by/4.0/>.

© The Author(s) 2023